Journal of Hazardous Materials 403 (2021) 124048

Contents lists available at ScienceDirect

Journal of Hazardous Materials

journal homepage: www.elsevier.com/locate/jhazmat

Metal–organic frameworks derived C/TiO_2 for visible light photocatalysis: Simple synthesis and contribution of carbon species

Xin He [a], Ming Wu [a], Zhimin Ao [a,*], Bo Lai [b], Yanbo Zhou [c], Taicheng An [a], Shaobin Wang [d,*]

[a] Guangdong Key Laboratory of Environmental Catalysis and Health Risk Control, Guangzhou Key Laboratory Environmental Catalysis and Pollution Control, School of Environmental Science and Engineering, Institute of Environmental Health and Pollution Control, Guangdong University of Technology, Guangzhou 510006, China
[b] State Key Laboratory of Hydraulics and Mountain River Engineering, College of Architecture and Environment, Sichuan University, Chengdu 610065, China
[c] State Environmental Protection Key Laboratory of Environmental Risk Assessment and Control on Chemical Process, East China University of Science and Technology, No. 130 Meilong Road, Xuhui District, Shanghai 200237, China
[d] School of Chemical Engineering and Advanced Materials, University of Adelaide, Adelaide, SA 5005, Australia

ARTICLE INFO

Keywords:
MIL-125(Ti)
Carbon doping
TiO_2
Photocatalysis
Bisphenol A

ABSTRACT

A series of in-situ carbon-doped TiO_2 (C_x/TiO_2) composites with a porous and crystalline structure were successfully synthesized via one-step and low-temperature calcination of titanium metal–organic framework (MOF), MIL-125(Ti). The resultant materials were comprehensively investigated by X-ray diffraction (XRD), scanning electron microscopy (SEM), X-ray photoelectron spectroscopy (XPS), N_2 adsorption–desorption measurements, UV–vis diffuse reflectance spectrum (DRS), photoluminescence (PL) spectra and photoelectrochemical measurements, and their photocatalytic activities for bisphenol A (BPA) degradation were assessed. Compared with the benchmark TiO_2 photocatalyst (P25), the C_x/TiO_2 composite material with high specific surface, lower band gap, and reduced photogenerated electron hole ratio exhibited outstanding photodegradation activity and durability for BPA, which could be attributed to the combined effect of co-doping of multiple carbon species (substituent carbon and carbonate) and porous structure. During BPA degradation, the holes and superoxide radicals were the primary role oxidative species in the reaction process. Therefore, this new efficient photocatalyst is promising candidate for photodegradation of organic pollutants.

1. Introduction

Industrial wastewater contains various organic pollutants with toxicity, chemical stability and bioaccumulation, which may cause adverse effects to the ecological environment and human health (Casillas et al., 2017; Li et al., 2016; Cui et al., 2014). To remediate the organic pollutants in industrial wastewater, numerous methods have been explored, including physical adsorption (Hu et al., 2011), bio-degradation (Huang et al., 2017), chemical reactions (Huang et al., 2015; Cheng et al., 2016; Li et al., 2019), and photocatalysis (Wang et al., 2020; Wu et al., 2020, 2018). Photocatalysis by solar energy is regarded as a promising method (Liu et al., 2019; Yu et al., 2019; Wang et al., 2017). Unlike traditional treatment methods, photocatalysis can remove low concentrated contaminants without secondary treatment. Among different photocatalysts, TiO_2 has been regarded as among the most appealing photocatalysts attributable to its environmental friendliness, non-toxicity, high catalytic activity, affordable and chemical stability and et al. (Wang et al., 2017; Zhou et al., 2018; Etacheri et al., 2015). Unfortunately, commercial TiO_2 still suffer the drawback of weak adsorption in visible light, low efficiency, and rapid recombination of photogenerated carriers (Wang et al., 2017), which largely hampers its feasible application in wastewater treatment. Consequently, various modification strategies, including semiconductor coupling (Lu et al., 2018), transition metallic/non-metallic doping (Etacheri et al., 2015; Liao et al., 2017), self-assembly (Zhang et al., 2015) and template preparation (Zhou et al., 2018) have been developed to improve its visible light utilization and the photocatalytic performance. Among them, non-metal doping for TiO_2 is generally considered to be a good choice for realizing the visible-light response and reducing the photo-excited carrier recombination ability (Zhang et al., 2015, 2014; Gu et al., 2016). Metal-free dopants adjust the valence band and band gap of TiO_2 by affecting the O 2p orbital (Sun and Zhang, 2016). In particular, carbon doping induced by carbonate groups has attracted great attention in heterogeneous photocatalysis for their visible light response,

* Corresponding authors.
E-mail addresses: zhimin.ao@gdut.edu.cn (Z. Ao), shaobin.wang@adelaide.edu.au (S. Wang).

https://doi.org/10.1016/j.jhazmat.2020.124048
Received 9 December 2019; Received in revised form 12 September 2020; Accepted 14 September 2020
Available online 19 September 2020

sensitized TiO_2 and narrow bandgap (Sankar Ganesh et al., 2018; Khalid et al., 2017; Jia et al., 2018; Wang et al., 2018). Due to the porosity and good electric conductivity of the carbon support and the close interfacial electronic contact between carbon and TiO_2 components, which can effectively promote electron-holes separation of electron holes, and hence improving the photocatalytic properties (Yu et al., 2014; Guo et al., 2014).

Lots of strategies have been employed to develop carbon-TiO_2 materials, such as using a sol–gel routes with carbon precursors (Shu Wang et al., 2014), solvothermal synthesis (Khalid et al., 2017), high-temperature annealing TiO_2-carbon materials (Li et al., 2012) and electrospinning method (Wang et al., 2018). For example, Zhang et al. (2015) devised prepared carbon doped TiO_2 photocatalyst through template-guided self-assembly using cationic polystyrene spheres as the template and carbon source, and Li et al. (2012) synthesized TiO_2--carbon composites by adding phenylphosphonic acid as carbon source for photocatalysis application. However, traditional methods show some drawbacks, such as high-temperature process accompanied by the phase transition of TiO_2, external carbon precursors adding, complex preparation processes, small specific surface areas and low photocatalytic activity. Therefore, facile methods to prepare carbon-doped TiO_2 with high surface area are highly needed.

Recently, metal–organic frameworks (MOFs) are an emerging class of porous materials, comprising of metal centers and coordinated organic linkers, attract intensive attentions for their highly adjustable pore size and shape, diverse structures and various functionalities (Gang Huang et al., 2015; Ma et al., 2017; Zhang and Lin, 2014). Synthesis of carbon doped TiO_2 from MOFs is considered as a promising process. Moreover, MOFs are utilized as sacrificial precursors for forming the uniform distribution of elements, large specific surface area, highly dispersed active sites and controllable compositions. As one of the MOF structures, MIL-125(Ti) is a good precursor to synthesize carbon/TiO_2 composites because it does not require any functional precursors or post-treatment. Li et al. (2017) obtained mixed-phase TiO_2 from MIL-125(Ti) through two-step calcination, which was utilized for photocatalytic degradation of nitrobenzene. Shi et al. (2016) synthesized TiO_2@C composites as electrode material through two-step method. As previously reported, a variety of porous TiO_2-carbon composite was also obtained via thermolysis of MIL-125(Ti) at high temperatures, showing excellent performance in microwave absorption and photocatalytic degradation of dyes (Guo et al., 2014; Ma et al., 2017). However, there is no report that carbon-doped TiO_2 (C_x/TiO_2, x is calcination time) was synthesized by the one-pot calcination of MIL-125(Ti) at low temperature, and their photoactivities for degrading organic pollutants by visible light is also needed to investigate.

Herein, we synthesized the C_x/TiO_2 hybrids via simple calcination of MIL-125(Ti) at low temperature and investigated their outstanding photodegradation efficiency via degrading bisphenol A (BPA) induced by visible light. The as-acquired photocatalysts were characterized by X-ray diffraction (XRD), scanning electron microscopy (SEM), X-ray photoelectron spectroscopy (XPS), N_2 adsorption–desorption measurements, UV–vis diffuse reflectance spectrum (UV–vis DRS), photoluminescence (PL) spectra, and photoelectrochemical experiments for investigation of materials' carriers separation ability. To confirm the contribution of reactive oxygen species (ROS) during the degradation process, electron paramagnetic resonance (EPR) and trapping experiment were carried out, and photocatalytic reaction sequence of C_{8h}/TiO_2 was suggested.

2. Experimental

2.1. Materials

Titanium tetraisopropanolate (98%, Ti-$(OC_3H_7)_4$) and Terephthalic acid (99%, TA) were provided from J&K Scientific Ltd. Disodium ethylenediaminetetraacetate (EDTA-2Na), 5,5-dimethyl-1-pyrroline N-oxide (DMPO), isopropanol (IPA), Nitrotetrazolium Blue chloride (NBT) and 1,4-benzoquinone (BQ) were provided by Aladdin Industrial Inc. Commercial TiO_2 (P25, 99.5%) were purchased from Aladdin Chemistry Reagent Co., Ltd. *N*,*N*-diethyl-1,4-phenylenediamine sulfate (DPD, 97%), peroxidase (POD, horseradish), dibasic sodium phosphate heptahydrate and monobasic sodium phosphate were provided by Sigma-Aldrich, Inc. All reagents were of analytical grade and used without further treatment.

2.2. Samples preparation

Preparation of MIL-125(Ti): MIL-125(Ti) was synthesized via a solvothermal technique based on the previously documented method (Ahmed et al., 2017). Briefly, 9 mmol of titanium tetraisopropanolate and 15 mmol of TA were added into a solvent containing methanol (5 mL) and *N*,*N*-dimethyl formamide (DMF, 45 mL). After ultrasonication and dissolution, the homogeneous mixtures were transferred to a Teflon-lined steel autoclave with heating 16 h under 150 °C. Upon cooling, the resultant precipitate was collected via centrifugation, followed by washing a few times with methanol and DMF.

Preparation of C_x/TiO_2 composites: The above-prepared MIL-125(Ti) at 0.2 g was annealed 2 h under 350 °C in a ceramic boat, and then a sample (C_{2h}/TiO_2) was achieved after natural cooling. Samples were prepared by the aforesaid method denoted as C_x/TiO_2 samples, where x indicated the calcination time (2 h, 5 h, 8 h and 10 h). The photoelectrochemical measurements were carried out according Text S1 (supporting information).

2.3. Characterization

X-ray diffraction (XRD) patterns was measured on a D/MAX-Ultima IV equipped with Cu Kα X-ray radiation. Thermogravimetric analysis (TGA) and differential scanning calorimetry (DSC) was conducted using a Mettler Toledo apparatus in air with a cooling/heating rate of 10 °C min^{-1}. Scanning electron microscopy (SEM, Hitach SU8220) and transmission electron microscopy (TEM, FEI Tecnai-F20) equipped with an Energy Dispersion Spectrometer (EDS) were used to investigate the morphology and microstructure of the samples. UV–vis diffuse reflectance spectra (DRS) were documented on an Agilent Carry 300 spectrophotometer. X-ray photoelectron spectroscopy (XPS, Perkin-Elmer Corporation, USA) examinations were conducted using ESCALab250 spectrometer. The Brunauer–Emmett–Teller (BET) specific surface areas and pore size distribution were measured via N_2 adsorption and desorption isotherms with a Micromeritics ASAP 2020M apparatus. Photoluminescence (PL) spectra were characterized on a HORIBA Fluorolog-3 fluorescence spectrometer. The electron paramagnetic resonance (EPR) signal spin-trapped by reagent 5,5-dimethyl-L-pyrroline N-oxide (DMPO) was obtained with a Bruker EMXPlus-10/12 EPR spectrometer.

2.4. Photocatalytic degradation experiments

Photocatalytic activities of synthesized specimens were assessed by degrading BPA under visible light illumination. A 300 W Xenon lamp (Microsolar 300, Beijing Perfectlight Technology Co., Ltd., China) equipment with a UV cut filter ($\lambda > 420$ nm) was the light source (Fig. S1), and its irradiation intensity was 305 mW cm^{-2}. A certain amount catalyst (0.02 g) was placed into 100 mL BPA aqueous solution (20 mg/L) in a container with cooling water jacked outside. Subsequently the suspension was stirred for 60 min under dark conditions to achieve the adsorption–desorption equilibrium. Finally, the dispersed suspension was irradiated with visible light, and the temperature of the suspension increased from 25 °C to 28 °C. At particular intervals of time, a small aliquot of the suspension was filtered through a syringe with polytetrafluoroethylene membrane of a 0.22 μm pore size, and then transferred to a high-performance liquid chromatography (HPLC) vial

for further analysis. All experiments were carried out in triplicate, and the mean and standard deviations were provided.

3. Results and discussion

3.1. Characterizations of photocatalysts

Fig. 1a displays the XRD pattern of as-synthesized MIL-125(Ti) corresponding to the diffraction pattern of simulated MIL-125(Ti) in reported work, in agreement with the crystal structure (Meenakshi Dan-Hardi et al., 2009), indicating successful formation of pure phase MIL-125(Ti) structure. As depicted in Fig. 1b, XRD peaks of the as-obtained C_x/TiO_2 materials at different calcination time show the typical anatase crystal. The intensity of characteristic diffraction planes of anatase C_x/TiO_2 increase as the calcination time increasing. C_{2h}/TiO_2 has almost no obvious peaks from its XRD pattern, which indicates an amorphous structure of the C_{2h}/TiO_2. When increasing calcination time, the surface amorphous carbon or organic groups were burned out and crystalline anatase TiO_2 is found in C_x/TiO_2 samples (x = 5 h, 8 h and 10 h). All characteristic diffraction peaks of C_x/TiO_2 could be in accordance with anatase phase of TiO_2 crystal. (JCPDS 73–1764 (Liu et al., 2018)).

The morphology and structure of as-obtained products were observed through means of SEM and TEM. The morphology of C_x/TiO_2 samples is influenced by the calcination time. With analysis in Fig. 2a, C_{2h}/TiO_2 maintains the similar morphology as its matrix MOF (Fig. S2). As shown in Fig. 2b–d, crystalline TiO_2 appears in the samples at increasing calcination time, indicated by the spherical nanoparticles.

Similar phenomenon is also demonstrated in TEM images (Fig. 3), C_{2h}/TiO_2 has an amorphous structure with no lattice fringes structure (Fig. 3a), well consistent with above result from XRD. As illustrated in Fig. 3c and d, the lattice fringes of crystalline nanoparticles become more clearly with increasing calcination time. The lattice distance of C_x/TiO_2 samples (x = 5 h, 8 h and 10 h) is ~0.35 nm, which is indicated as the (101) facets of anatase TiO_2 (Zhang et al., 2006). To further verify the inner structural features, the fast Fourier transform (FFT) was used to filter a selected region of the image (inset of Fig. 3g). The observed selected-area FFT pattern shows the spot pattern and a set of diffusing rings, which can correspond to anatase phase and amorphous structure, further confirming the existence of amorphous carbon dopants. Additionally, the EDS element mapping images of C_{8h}/TiO_2 (Fig. S3) further reveals that C element is evenly distributed over the TiO_2 matrix. The above observations demonstrate that the formation of amorphous carbon incorporated into highly crystalline anatase TiO_2.

TGA and DSC analysis were carried out to determine proper temperature for partial removal of organic groups in MIL-125(Ti) during thermal calcination. MIL-125(Ti) is stable with the temperature lower than 300 °C corresponded to the departure of absorbed water or other volatile compounds (Fig. S4). With increasing calcination temperature,

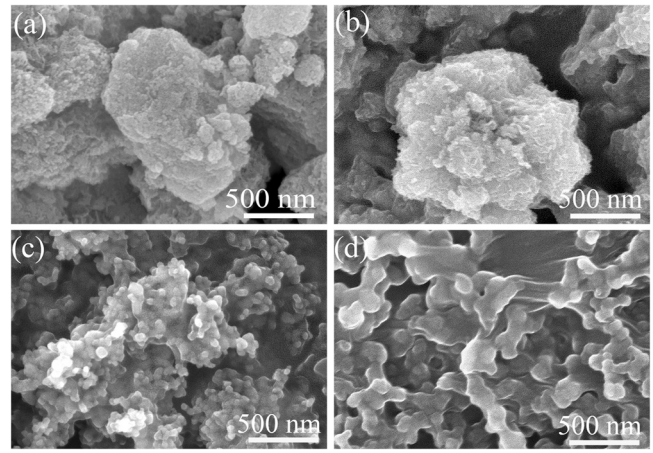

Fig. 2. SEM images of (a) C_{2h}/TiO_2, (b) C_{5h}/TiO_2, (c) C_{8h}/TiO_2, and (d) C_{10h}/TiO_2.

there is a dramatical weight loss of 35% occurred between 350 °C and 500 °C, related to the framework decomposition of MIL-125(Ti). The DSC profile showed that the two endothermic peaks at 353 °C and 466 °C are related to the decomposition and crystallization transformation of organic components, respectively (Liu et al., 2018). At calcination temperature 500 °C, organic groups of MIL-125(Ti) were totally removed to obtain TiO_2. To obtain similar morphology and porous structure of MIL-125(Ti), a relatively low temperature 350 °C was chosen to prepare C_x/TiO_2 composites in this work. This idea was verified by the SEM analysis, where the C_{2h}/TiO_2 sample inherited the same morphology of MIL-125(Ti) (Fig. 2a and Fig. S2). When increasing calcination time of MIL-125 (Ti), all calcined samples exhibited type-IV isotherms with hysteresis loops, indicating the presence of mesoporous structure for the C_x/TiO_2 samples, and the S_{BET} decreases from 358.9 to 147.0 $m^2\ g^{-1}$ with the average pore size increases from 5.7 to 13.0 nm (Fig. S5 and Table S1). In contrast to P25 (40.7 $m^2\ g^{-1}$), the obtained C_{8h}/TiO_2 shows a large surface area of 163.1 $m^2\ g^{-1}$, but it is lower than that of pure MIL-125(Ti) (762.2 $m^2\ g^{-1}$).

UV–vis DRS and photocurrent responses were performed to explore the optical absorption capacity and electronic properties of C_x/TiO_2 composites. C_{2h}/TiO_2 and C_{5h}/TiO_2 show a wide visible wavelength absorption (Fig. 4a), which are caused by the incorporation of carbonate species and additional organic groups remained in the samples. The disappearance of the organic groups could reduce the visible-light absorbance as demonstrated in C_x/TiO_2 samples (x = 8 h and 10 h), which still show higher visible light absorption compared with commercial P25, attributed by the carbon doping (Ivanov et al., 2016). In addition, the change in color of the samples from brown to beige may be

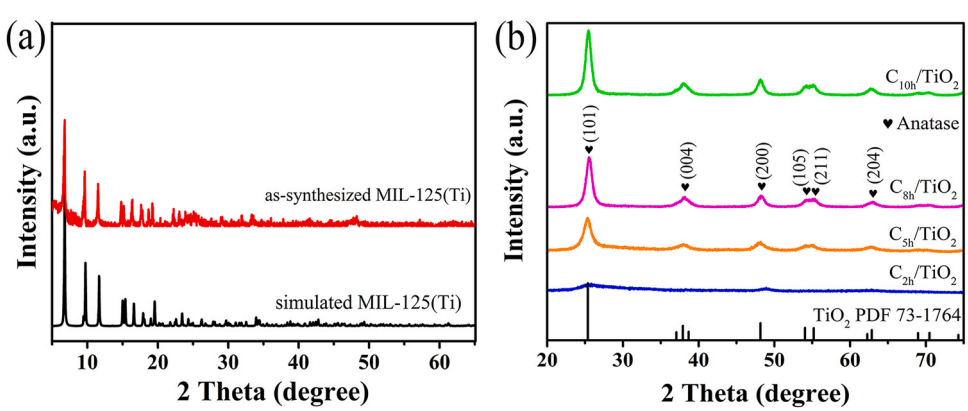

Fig. 1. (a) XRD patterns of as-synthesized MIL-125(Ti) and the simulated from crystal structure data, considering only framework atoms (i.e., contributions from solvent species within the cavities were excluded), (b) XRD patterns of C_x/TiO_2 samples.

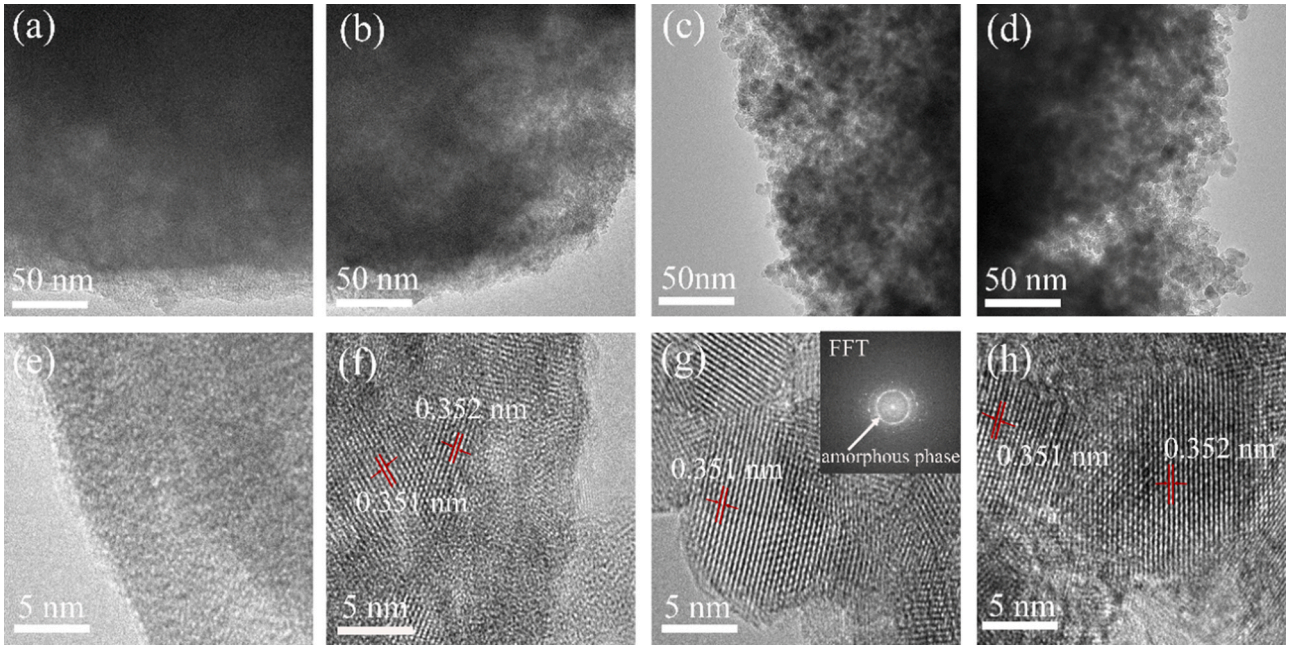

Fig. 3. Low- and high-magnification TEM images of C_{2h}/TiO_2 (a and e), C_{5h}/TiO_2 (b and f), C_{8h}/TiO_2 (c and g), and C_{10h}/TiO_2 (d and h) samples. The inset image of (g) is FFT analysis of C_{8h}/TiO_2.

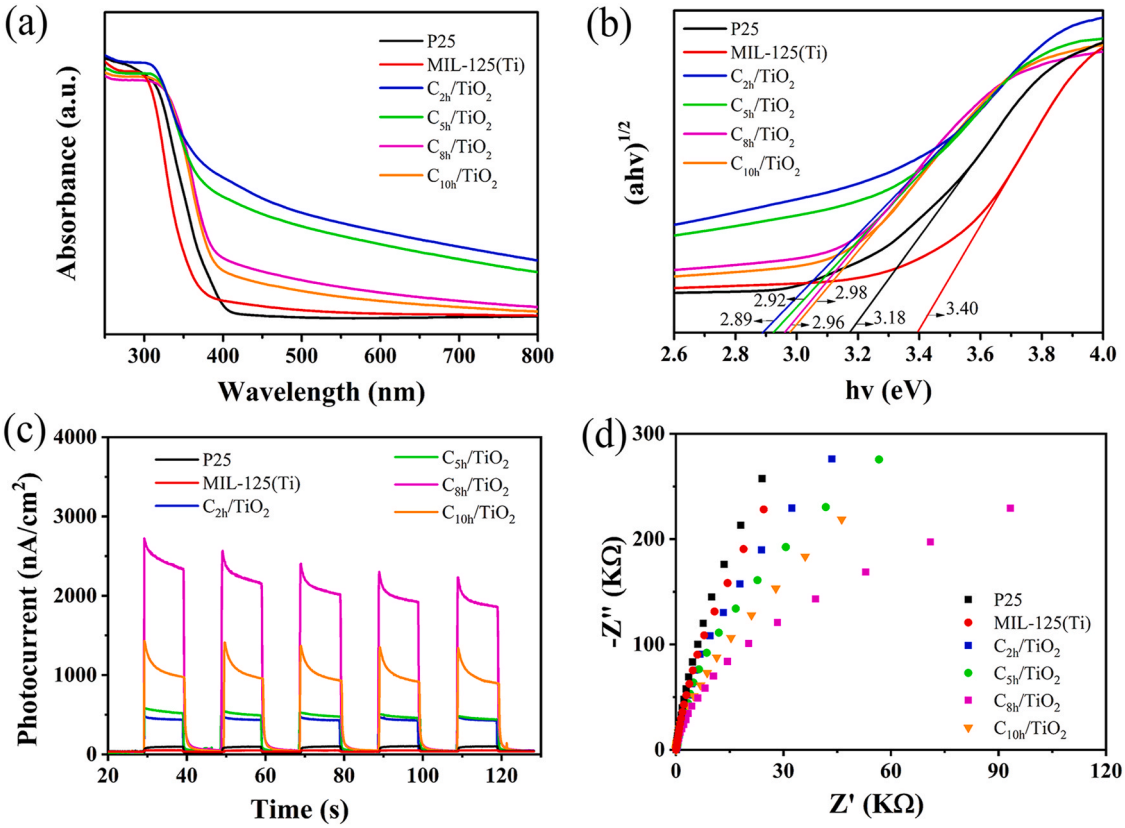

Fig. 4. (a) UV–vis DRS and (b) $(\alpha h\nu)^{1/2}$ vs. photon energy ($h\nu$) of P25, MIL-125 (Ti), C_x/TiO_2 samples, (c) photocurrent responses and (d) EIS Nyquist plots of P25, MIL-125(Ti), and C_x/TiO_2 composites.

related to the loss of carbon species in the C_x/TiO_2 samples (Fig. S6).

Meanwhile, according to Tauc plot (Fig. 4b), the calculated band gap of MIL-125(Ti), P25, C_{2h}/TiO_2, C_{5h}/TiO_2, C_{8h}/TiO_2 and C_{10h}/TiO_2 were estimated as 3.40, 3.18, 2.89, 2.92, 2.96 and 2.98 eV, respectively. C_x/TiO_2 samples show narrow bandgap attributing to the carbon doping, which is in accordance with the XPS results. In addition, carbon doping can decrease the recombination of photoinduced charge pairs and is beneficial to the formation of oxygen vacancies (Shao et al., 2015; Parayil et al., 2013). Hence, the C_{8h}/TiO_2 shows a much lower emission peaks intensity than MIL-125(Ti) and P25 with analysis from PL spectra

(Fig. S7). Moreover, photoelectrochemical performance of samples have been tested for analyzing the photogenerated electron-hole pairs beneath visible light illumination. A higher current density was achieved by C_{8h}/TiO_2 than the other samples as exhibited in Fig. 4c, implying the enhanced electron-hole pairs generation. The charge transfer resistance of C_x/TiO_2 was also determined based on the EIS Nyquist analysis (Fig. 4d). C_x/TiO_2 photocatalysts with smaller radius exhibited better electronic conductivity than that of P25, and the C_{8h}/TiO_2 displayed the smallest radius, thereby revealing a faster interface charge transportations caused by the amorphous carbon doping (Wang et al., 2015). Therefore, the enhanced photoelectrical activity of C_{8h}/TiO_2 suggests that the amorphous carbon doping could promote effective transfer and separation of electron-hole pairs.

The surface characteristics of the C_x/TiO_2 samples were ascertained via XPS measurement. As exhibited in Fig. S8, titanium, oxygen and carbon elements were detected in C_{2h}/TiO_2, C_{5h}/TiO_2, C_{8h}/TiO_2 and C_{10h}/TiO_2 samples. Fig. 5a shows three peaks in high resolution C1s spectrum of C_x/TiO_2 composites. The C1s peak at 284.8 eV is feature, corresponding to C–C bond overlapping with graphite-like C. The larger intensity is an important index for incorporating carbonate groups into TiO_2 (Liu et al., 2014). The intensities of major peak of C_x/TiO_2 samples gradually decreased after increasing calcination time (Fig. 5a), indicating that more graphite-like sp^2 carbon was found in C_{2h}/TiO_2 samples. Two peaks at about 286 eV and 288 eV are ascribed separately to C–O, C=O and/or COO bonds, corresponding to the presence of carbonates in C_x/TiO_2 composites, which could reduce bandgap and elevated visible light absorption ability (Juming Liu et al., 2017), further supporting the UV–vis DRS results. Thus, the above XPS results demonstrated that carbonates were successfully doped into all four samples. The peak near 288 eV can also be assigned to the C–O bond, indicating that C substituted Ti in the TiO_2 lattice, thereby forming Ti-O-C structure in this catalyst (Yu et al., 2014; Kiran and Sampath, 2012). The peak appears around 288.7 eV is caused by the increase of carbonate groups as the calcination time increasing. Moreover, we also found that the relative content of C–O bonds gradually increased, while the relative content of C=O and/or COO bonds gradually decreased in C_x/TiO_2 with the calcination time from 5 h to 10 h (Table S2). In addition, the C1s binding energy peak of other samples was negatively shifted (0.3 eV) in contrast to C_{2h}/TiO_2, suggesting that surface oxygen species altered with the change of calcination time. And there was no characteristic peak of the Ti-C bond (281 eV) in the C 1s binding energy (Jia et al., 2018). Two XPS signals of Ti 2p (Fig. 5b) were observed around 458.8 eV and 464.4 eV, which are separately indexed to Ti $2p_{3/2}$ and Ti $2p_{1/2}$ of TiO_2 species (Xiang et al., 2010). Compared with C_{8h}/TiO_2, the peak position of C_{5h}/TiO_2 tends to shift to higher binding energy, which may be related to the excessive carbon species produced by the decomposition of amorphous carbon covering the sample surface (Wang et al., 2018). The peak intensity of Ti 2p core energy level of C_{8h}/TiO_2 and C_{10h}/TiO_2 was significantly enhanced and the peak position was obviously shifted to low energy (0.2 eV) for comparison of other C_x/TiO_2 composites, suggesting the possible formation of non-stoichiometric TiO_2 (oxygen vacancies) (Jia et al., 2018). The change of binding energy originated from the reduction of electron density of Ti nuclei through carbon doping (Wang et al., 2018). Moreover, the presence of the peak around 460 eV was associated with Ti-C bonds, demonstrating that C element doped on the anatase phases TiO_2 (Wang and Lim, 2010; Oseghe and Ofomaja, 2018). It can be seen that the relative content of Ti-C linkage in C_{8h}/TiO_2 was higher than C_{10h}/TiO_2 (Table S3). When analyzing high-resolution XPS spectrum of O 1s in Fig. 5c, three peaks can also be visualized, which could be attributed to Ti-O (around 530.0 eV), C–O bonds (around 531.3 eV), O–H bonds (around 532.4 eV), respectively. According to above results, it can be concluded that in-situ doping of carbon occurs during simple annealing of the MOF precursor, and the existence form of carbon species in the TiO_2 crystal lattice converts from carbonate species to the coexistence of carbonate and substituted carbon as the calcination time

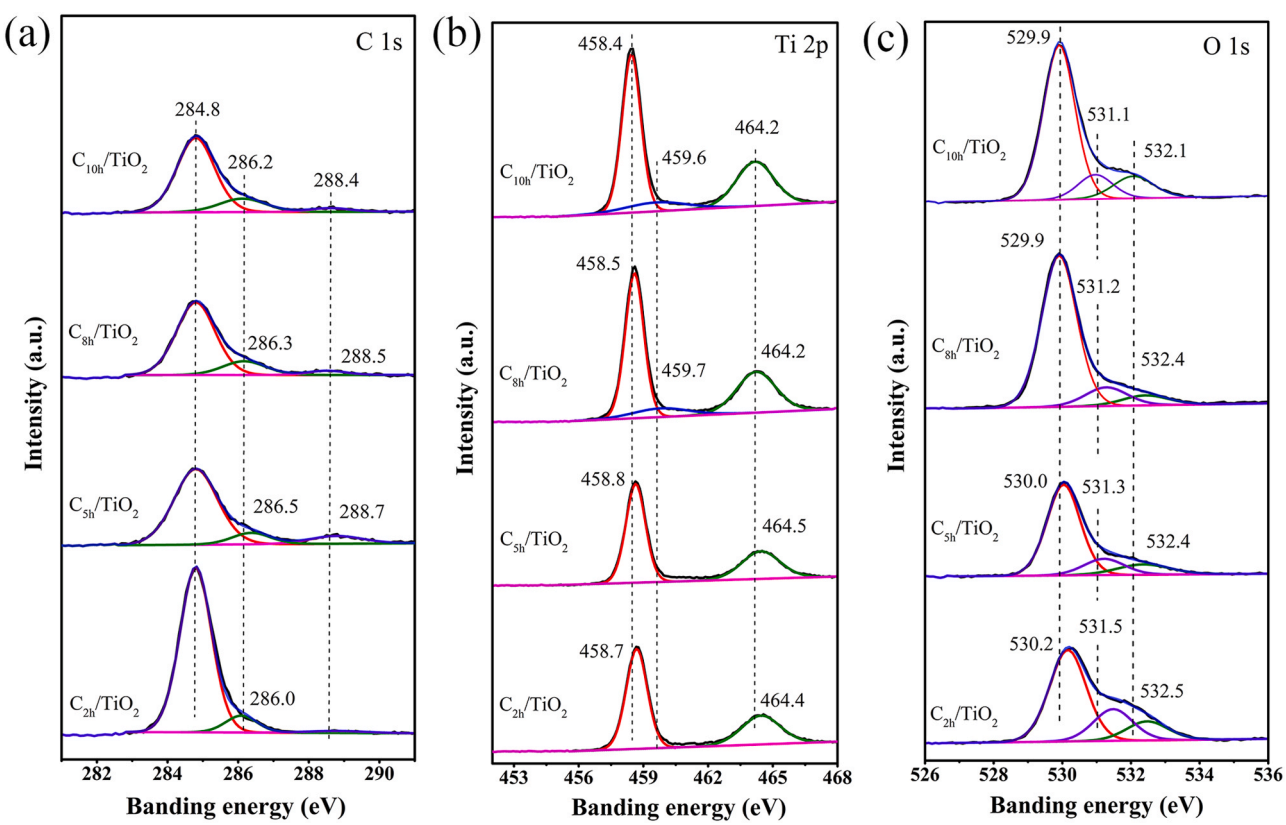

Fig. 5. XPS spectra of C_x/TiO_2 samples, (a) C 1s, (b) Ti 2p and (c) O 1s.

increasing. The synergistic impact of co-doping of multiple carbons (carbonate and substituted carbon) and improved absorption of visible light may lead to the elevated photocatalytic activity.

3.2. Photocatalytic performance evaluation

The photocatalytic activities of prepared C_x/TiO_2 to visible light induced BPA degradation is shown in Fig. 6. From Fig. 6a, there was negligible photo decomposition of BPA without catalyst. It was found that all C_x/TiO_2 samples exhibited remarkably enhanced photo-degradation activity for BPA degradation compared to MIL-125(Ti) and P25. In particular, C_{8h}/TiO_2 achieved 98% removal rate of BPA after 180 min of irradiation. Meanwhile, photodegradation rates were calculated by a pseudo-first-order kinetics. The rate constants (k) were obtained by using Eq. (1):

$$ln\left(\frac{C_0}{C}\right) = kt \quad (1)$$

where k, C_0, and C are respectively reaction rate constant, initial BPA concentration, and actual BPA concentration at reaction time of t.

As clearly shown in Fig. 6b and Table S4, MIL-125(Ti) shows the lowest value (0.00167 min^{-1}), while C_x/TiO_2 samples show much higher reaction rates. In particular, the reaction rate (0.01887 min^{-1}) of C_{8h}/TiO_2 is 10.3 times higher than that of MIL-125(Ti), and improved 9.6 times compared with P25 (0.00178 min^{-1}). This indicates that the combine effect of co-doping of multi carbon species and porous structure are beneficial to the enhanced photocatalytic performance. Meanwhile, some other C/TiO_2 systems reported for photodegradation are listed in Table 1. We can find that C_{8h}/TiO_2 shows an excellent photodegradation ability compared with other photocatalysts. In consideration of materials properties, we find that the crystallization and size of the nanoparticles can also affect photocatalytic performance (Valero-Romero et al., 2019). The photocatalytic activity of amorphous C_{2h}/TiO_2 with wide light absorption is also lower than that of C_x/TiO_2 (x = 5 h, 8 h and 10 h) samples. In addition, C_{8h}/TiO_2 shows a better photodegradation efficiency in comparison with C_{10h}/TiO_2, but the nanoparticle size of C_{8h}/TiO_2 is lower than that of C_{10h}/TiO_2 (Fig. 2c and d). Therefore, C_{8h}/TiO_2 exhibited the superior photocatalytic BPA degradation performances under visible light illumination.

Recycling tests were conducted to evaluate durability (Fig. S9), degradation rate of BPA by C_{8h}/TiO_2 only slightly declined after four runs of photo-degradation reaction. After the 4th recycling experiment, C_{8h}/TiO_2 could still degrade 84% BPA far outperformed the P25 (27%) or MIL-125(Ti) (24%). Meanwhile, the crystal structure of C_{8h}/TiO_2 is also very stable after the cycling experiment (Fig. S10).

Table 1
Photocatalyst of C-doped TiO_2 using different methods.

Catalyst	Carbon source	S_{BET} (m^2 g^{-1})	Degradation target	Reference
C_{8h}/TiO_2	MIL-125(Ti)	163.1	100% BPA was moved after 150 min under visible light	This work
Carbon-doped TiO_2	Carbon nanofibrous	233	94% RhB was moved after 150 min under visible light	Song et al., 2018
C-doped TiO_2	Ethylene glycol	/	100% RhB was moved after 120 min under UV light	Duan et al., 2018
C-doped hollow TiO_2	Cationic polystyrene spheres	17.6	99% RhB was moved after 40 min under visible light	Zhang et al., 2015
C-doped TiO_2	Titanium carbide	12	99% MB was moved after 120 min under visible light	Yu et al., 2011
C-doped TiO_2	Pine cone	8.3	70% TA was moved after 120 min under visible-LED light	Oseghe and Ofomaja, 2018
Carbon/ TiO_2	rice husk	124	75% BPA was moved after 300 min under UV light	Kim et al., 2010
TiO_x/C	MIL-125(Ti)	329	38.8% MB was moved after 60 min under UV light	Guo et al., 2014

3.3. Investigation of the effect of different scavengers

The produced generation of ROS during the photocatalytic degradation process were determined by trapping experiments. The influences of different scavengers on BPA degradation by C_{8h}/TiO_2 are illustrated in Fig. 7a and b. After adding $AgNO_3$, an electron capturer, the BPA removal efficiency decreased to 75.07%. The decrease of the amount of electrons leads to the reduction of the ROS such as $\bullet O_2^-$, which inhibits the degradation rate. The BPA degradation efficiency was greatly inhibited with adding EDTA-2Na or BQ. Specifically, the BPA removal efficiency in C_{8h}/TiO_2 system decreased from 98.83% to 5.29% and 12.24% respectively in the presence of EDTA and BQ, demonstrating that $\bullet O_2^-$ and h^+ were the predominant ROS. However, the BPA degradation efficiency exhibited no obvious decrease after IPA adding, suggesting the little contribution of •OH species in BPA degradation. Therefore, the h^+ and $\bullet O_2^-$ radicals acted as dominant reactive species generated, while •OH radicals had a smaller contribution in

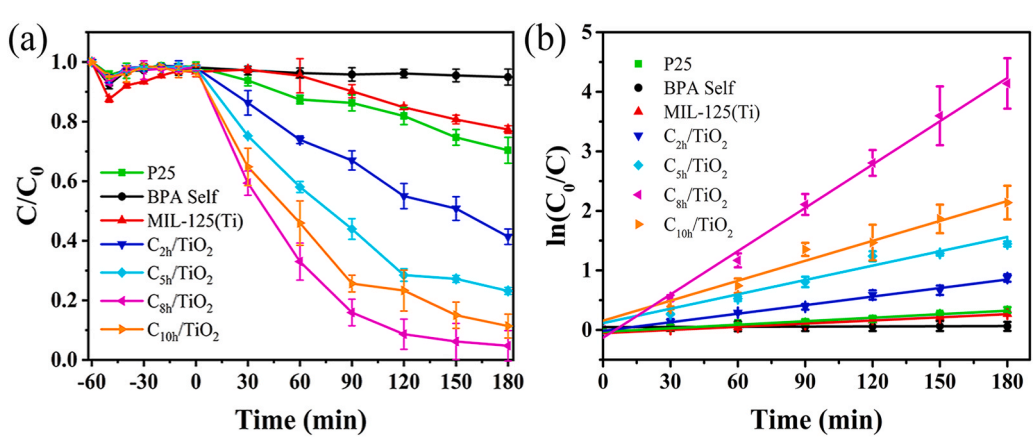

Fig. 6. Photocatalytic activities of (a) BPA degradation profiles and (b) related kinetics over MIL-125(Ti), P25, C_{2h}/TiO_2, C_{5h}/TiO_2, C_{8h}/TiO_2 and C_{10h}/TiO_2 samples under visible light irradiation.

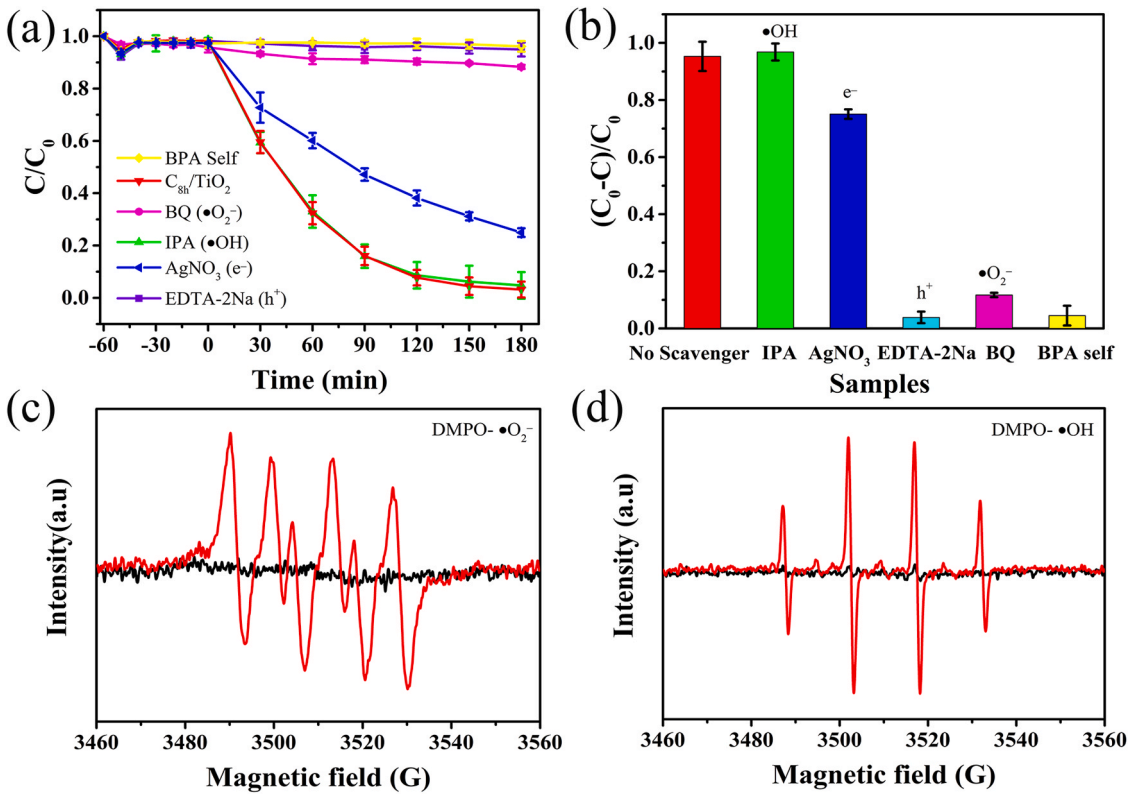

Fig. 7. (a) Effect of different scavengers on photocatalytic degradation of BPA by C_{8h}/TiO_2 under visible light irradiation; (b) the corresponding reaction constants. (IPA: 10 mM, EDTA-2Na, 10 mM, BQ: 10 mM, $AgNO_3$: 10 mM, catalyst: 20 mg, BPA: 100 mL 20 mg/L. (c) EPR signals of C_{8h}/TiO_2 for DMPO-•O_2^- formed in irradiated methanol dispersion, and (d) DMPO-•OH formed in irradiated H_2O dispersion.

photocatalytic reaction.

EPR spectroscopy was utilized to validate the formation of active radicals, •O_2^- and •OH radicals with quencher DMPO. As depicted in Fig. 7c and d, there is no signal of •OH and •O_2^- radicals under dark conditions, while the characteristic peaks corresponding to DMPO-•O_2^- adduct for C_{8h}/TiO_2 are produced after switching on the visible light. Meanwhile, the signal of •OH radicals were also detected beneath visible light irradiation. Hence, the EPR results further evidenced that limited •OH radicals were generated in the C_{8h}/TiO_2 system, while little influence of IPA addition on •OH radical detection might be caused by the much low concentration of •OH radicals.

Mott–Schottky (MS) plots was used for estimating the band structure feature of C_{8h}/TiO_2. C_{8h}/TiO_2 can be considered as an n-type semiconductor according to the positive slope of MS curve (Fig. S11) (Yu et al., 2016). The estimated flat band potentials for C_{8h}/TiO_2 is − 0.79 V vs. Ag/AgCl electrode, which can be converted to − 0.55 V vs. normal hydrogen electrode (NHE) (Lin et al., 2019). In general, the conduction band (E_{CB}) edge of the typical n-type semiconductors is 0.20 V below its flat band potential (Yu et al., 2016). Then, the E_{CB} values of C_{8h}/TiO_2 was determined to be − 0.75 V vs. NHE. The valence band (E_{VB}) potential of the C_{8h}/TiO_2 can be expressed by using Eq. (2):

$$E_{CB} = E_{VB} - E_g \tag{2}$$

In this way, E_{VB} position of C_{8h}/TiO_2 was calculated to be + 2.21 V vs. NHE. The C_{8h}/TiO_2 showed a more negative E_{CB} position (− 0.75 V vs. NHE) compared with the potential of O_2/•O_2^- (− 0.33 V vs. NHE), suggesting that photo-generated electrons of C_{8h}/TiO_2 could capture dissolved O_2 to generate •O_2^- (Lu et al., 2017). However, the E_{VB} value of C_{8h}/TiO_2 is + 2.21 V vs. NHE, which is below the OH^-/•OH (+ 2.40 V vs. NHE) and H_2O/•OH (+ 2.38 V vs. NHE), indicating that photo-generated holes of C_{8h}/TiO_2 could not directly yield •OH radicals (Yu et al., 2016; Lu et al., 2017), while •O_2^- can be partially converted to produce a small number of •OH through the following reactions: $\bullet O_2^- + e^- + 2H^+ \rightarrow H_2O_2$, $H_2O_2 + e^- \rightarrow \bullet OH + OH^-$. This can be further confirmed by the quantitative analysis of reactive oxygen species in Text S2 (supporting information). The NBT probe molecule specifically reacted with •O_2^- to form precipitate upon visible light excitation, and a decrease in absorbance at 260 nm was observed after photocatalytic degradation (Fig. S12a) (Xia et al., 2015). The results using TA as a probe showed that the increasing intensity of the fluorescence emitted at 427 nm, confirming the •OH radicals were involved in the photocatalytic reaction (Fig. S12c) (Zhang et al., 2015; Moon et al., 2014). However, the concentration of H_2O_2 increases firstly and then gradually decreases was observed in Fig. S12b. Combined with the trapping experimental results, this may indicated that the holes enhanced charge carrier separation and produced more photoelectrons. Therefore, more produced •O_2^- would reactions with H^+ to produce H_2O_2 through one-electron reduction process. Then, H_2O_2 could be transformed into •OH via a one-electron reduction process, resulting in an increase in H_2O_2 consumption. Based on the discussion above, an underlying reaction sequence of photocatalytic over C_{8h}/TiO_2 sample under visible light is proposed in Fig. 8. During photocatalytic reaction, main active species including •O_2^- and h^+ together with little amount •OH active species are generated for BPA degradation. Meanwhile, the remarkable photocatalytic performance of C_{8h}/TiO_2 sample is attributed to lower bandgap for broadening light absorption edge and a high specific surface area compared with commercial P25.

4. Conclusions

In-situ carbon-doped TiO_2 (C_x/TiO_2) composites were successfully synthesized by annealing MIL-125(Ti) at low temperature. C_{8h}/TiO_2 shows 9.6 times higher photocatalytic BPA degradation rate than the commercial P25 under visible light irradiation. This excellent

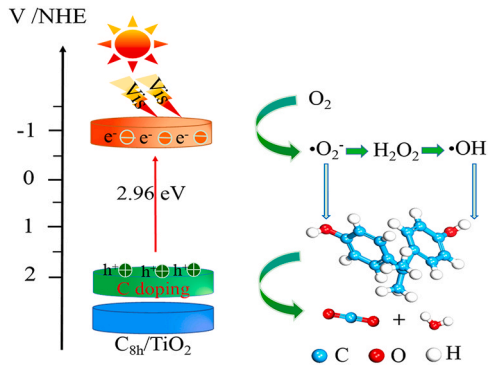

Fig. 8. A schematic illustration of photocatalytic reaction sequence of C_{8h}/TiO_2.

photocatalytic performance is closely related to the morphology, crystallinity and structure of the catalysts. The unique porous structure from MOFs can enhance the light collection through the reflection effect. In addition, the co-doping of carbonate and substituted carbon can accelerate the separation of photogenerated charges and reduce the band gap. Furthermore, $\bullet O_2^-$ and h^+ were the main reactive species, which are responsible for the BPA degradation. This work presents a facile and versatile strategy for the preparation of photocatalysts that hold great promise in the treatment of organic wastes for environmental remediation.

CRediT authorship contribution statement

Xin He: Investigation, Data curation, Formal analysis, Writing - original draft. **Ming Wu:** Data curation, Writing - reviewing & editing. **Bo Lai:** Writing - reviewing & editing. **Yanbo Zhou:** Writing - reviewing & editing. **Zhimin Ao:** Conceptualization, Supervision, Funding acquisition, Validation, Writing - reviewing & editing. **Taicheng An:** Writing - reviewing & editing, Supervision. **Shaobin Wang:** Conceptualization, Supervision, Writing - reviewing & editing.

Declaration of Competing Interest

The authors declare that they have no known competing financial interests or personal relationships that could have appeared to influence the work reported in this paper.

Acknowledgments

This work is financially supported by the National Natural Science Foundation of China (Grant Nos. 21777033, 21806023, 41425015), Science and Technology Program of Guangdong Province (2017B020216003), and the Innovation Team Project of Guangdong Provincial Department of Education (No. 2017KCXTD012).

Appendix A. Supporting information

Supplementary data associated with this article can be found in the online version at doi:10.1016/j.jhazmat.2020.123999.

References

Ahmed, I., Khan, N.A., Yoon, J.W., Chang, J.S., Jhung, S.H., 2017. Protonated MIL-125-NH_2: remarkable adsorbent for the removal of quinoline and indole from liquid fuel. ACS Appl. Mater. Interfaces 9, 20938–20946.

Casillas, J.E., Tzompantzi, F., Castellanos, S.G., Mendoza-Damián, G., Pérez-Hernández, R., López-Gaona, A., Barrera, A., 2017. Promotion effect of ZnO on the photocatalytic activity of coupled Al_2O_3-Nd_2O_3-ZnO composites prepared by the sol-gel method in the degradation of phenol. Appl. Catal. B Environ. 208, 161–170.

Cheng, M., Zeng, G., Huang, D., Lai, C., Xu, P., Zhang, C., Liu, Y., Wan, J., Gong, X., Zhu, Y., 2016. Degradation of atrazine by a novel Fenton-like process and assessment the influence on the treated soil. J. Hazard. Mater. 312, 184–191.

Cui, W., An, W., Liu, L., Hu, J., Liang, Y., 2014. Novel Cu_2O quantum dots coupled flower-like BiOBr for enhanced photocatalytic degradation of organic contaminant. J. Hazard. Mater. 280, 417–427.

Duan, Y., Chen, X., Zhang, X., Xiang, W., Wu, C., 2018. Influence of carbon source on the anatase and brookite mixed phase of the C-doped TiO_2 nanoparticles and their photocatalytic activity. Solid State Sci. 86, 12–18.

Etacheri, V., Di Valentin, C., Schneider, J., Bahnemann, D., Pillai, S.C., 2015. Visible-light activation of TiO_2 photocatalysts: advances in theory and experiments. J. Photochem. Photobiol. C Photochem. Rev. 25, 1–29.

Gang Huang, F.Z., Du, Xinchuan, Qin, Yuling, Yin, Dongming, Wang, Limin, 2015. Metal organic frameworks route to in situ insertion of multiwalled carbon nanotubes in Co_3O_4 polyhedra as anode materials for lithium-ion batteries. ACS Nano 9, 1592–1599.

Guo, Z., Cheng, J.K., Hu, Z., Zhang, M., Xu, Q., Kang, Z., Zhao, D., 2014. Metal-organic frameworks (MOFs) as precursors towards TiO_x/C composites for photodegradation of organic dye. RSC Adv. 4, 34221–34225.

Gu, Y., Cheng, K., Wu, Y.-n, Wang, Y., Morlay, C., Li, F., 2016. Metal–organic framework-templated synthesis of bifunctional N-doped TiO_2–carbon nanotablets via solid-state thermolysis. ACS Sustain. Chem. Eng. 4, 6744–6753.

Huang, D., Liu, L., Zeng, G., Xu, P., Huang, C., Deng, L., Wang, R., Wan, J., 2017. The effects of rice straw biochar on indigenous microbial community and enzymes activity in heavy metal-contaminated sediment. Chemosphere 174, 545–553.

Huang, D.L., Wang, R.Z., Liu, Y.G., Zeng, G.M., Lai, C., Xu, P., Lu, B.A., Xu, J.J., Wang, C., Huang, C., 2015. Application of molecularly imprinted polymers in wastewater treatment: a review. Environ. Sci. Pollut. Res. Int. 22, 963–977.

Hu, X.J., Wang, J.S., Liu, Y.G., Li, X., Zeng, G.M., Bao, Z.L., Zeng, X.X., Chen, A.W., Long, F., 2011. Adsorption of chromium (VI) by ethylenediamine-modified cross-linked magnetic chitosan resin: isotherms, kinetics and thermodynamics. J. Hazard. Mater. 185, 306–314.

Ivanov, S., Barylyak, A., Besaha, K., Bund, A., Bobitski, Y., Wojnarowska-Nowak, R., Yaremchuk, I., Kus-Liskiewicz, M., 2016. Synthesis, characterization, and photocatalytic properties of sulfur- and carbon-codoped TiO_2 nanoparticles. Nanoscale Res. Lett. 11, 140.

Jia, G., Wang, Y., Cui, X., Zheng, W., 2018. Highly carbon-doped TiO_2 derived from MXene boosting the photocatalytic hydrogen evolution. ACS Sustain. Chem. Eng. 6, 13480–13486.

Juming Liu, L.H., An, Ning, Xing, Lei, Ma, Huiyan, Cheng, Lin, Yang, Jucai, Zhang, Qiancheng, 2017. Enhanced visible-light photocatalytic activity of carbonate-doped anatase TiO_2 based on the electron-withdrawing bidentate carboxylate linkage. Appl. Catal. B Environ. 202, 642–652.

Khalid, N.R., Majid, A., Tahir, M.B., Niaz, N.A., Khalid, S., 2017. Carbonaceous-TiO_2 nanomaterials for photocatalytic degradation of pollutants: a review. Ceram. Int. 43, 14552–14571.

Kim, J.-Y., Kwak, B.-S., Kang, M.-S., 2010. TiO_2/carbon composites prepared from rice husk and the removal of bisphenol a in photocatalytic liquid system. Bull. Korean Chem. Soc. 31, 344–350.

Kiran, V., Sampath, S., 2012. Enhanced Raman spectroscopy of molecules adsorbed on carbon-doped TiO_2 obtained from titanium carbide: a visible-light-assisted renewable substrate. ACS Appl. Mater. Interfaces 4, 3818–3828.

Li, J., Xu, X., Liu, X., Qin, W., Wang, M., Pan, L., 2017. Metal-organic frameworks derived cake-like anatase/rutile mixed phase TiO_2 for highly effificient photocatalysis. J. Alloy. Compd. 690, 640–646.

Liao, Y.T., Huang, Y.Y., Chen, H.M., Komaguchi, K., Hou, C.-H., Henzie, J., Yamauchi, Y., Ide, Y., Wu, K.C.W., 2017. Mesoporous TiO_2 embedded with a uniform distribution of CuO exhibit enhanced charge separation and photocatalytic efficiency. ACS Appl. Mater. Interfaces 9, 42425–42429.

Lin, Y., Wu, S., Yang, C., Chen, M., Li, X., 2019. Preparation of size-controlled silver phosphate catalysts and their enhanced photocatalysis performance via synergetic effect with MWCNTs and PANI. Appl. Catal. B Environ. 245, 71–86.

Liu, Z., Wu, Y., Chen, J., Li, Y., Zhao, J., Gao, K., Na, P., 2018. Effective elimination of As (iii)viasimultaneous photocatalytic oxidation and adsorption by a bifunctional cake-like TiO_2 derived from MIL-125(Ti). Catal. Sci. Technol. 8, 1936–1944.

Liu, W., Zhang, W., Liu, M., Du, P., Dang, C., Liang, J., Li, Y., 2019. Fabrication of niobium doped titanate nanoflakes with enhanced visible-light-driven photocatalytic activity for efficient ibuprofen degradation. Chin. Chem. Lett. 30, 2177–2180.

Liu, J., Zhang, Q., Yang, J., Ma, H., Tade, M.O., Wang, S., Liu, J., 2014. Facile synthesis of carbon-doped mesoporous anatase TiO_2 for the enhanced visible-light driven photocatalysis. Chem. Commun. 50, 13971–13974.

Li, J., Li, Y., Xiong, Z., Yao, G., Lai, B., 2019. The electrochemical advanced oxidation processes coupling of oxidants for organic pollutants degradation: a mini-review. Chin. Chem. Lett. 30, 2139–2146.

Li, S., Zhang, G., Wang, P., Zheng, H., Zheng, Y., 2016. Microwave-enhanced Mn-Fenton process for the removal of BPA in water. Chem. Eng. J. 294, 371–379.

Li, L., Zhu, Y., Lu, X., Wei, M., Zhuang, W., Yang, Z., Feng, X., 2012. Carbon heterogeneous surface modification on a mesoporous TiO_2-supported catalyst and its enhanced hydrodesulfurization performance. Chem. Commun. 48, 11525.

Lu, L., Wang, G., Zou, M., Wang, J., Li, J., 2018. Effects of calcining temperature on formation of hierarchical TiO_2/g-C_3N_4 hybrids as an effective Z-scheme heterojunction photocatalyst. Appl. Surf. Sci. 441, 1012–1023.

Lu, Z., Zeng, L., Song, W., Qin, Z., Zeng, D., Xie, C., 2017. In situ synthesis of C-TiO_2/g-C_3N_4 heterojunction nanocomposite as highly visible light active photocatalyst originated from effective interfacial charge transfer. Appl. Catal. B Environ. 202, 489–499.

Ma, J., Liu, W., Liang, X., Quan, B., Cheng, Y., Ji, G., Meng, W., 2017. Nanoporous TiO_2/C composites synthesized from directly pyrolysis of a Ti-based MOFs MIL-125(Ti) for efficient microwave absorption. J. Alloy. Compd. 728, 138–144.
Meenakshi Dan-Hardi, C.S., Frot, Théo, Rozes, Laurence, Maurin, Guillaume, Sanchez, Clément, Férey, G.érard, 2009. A new photoactive crystalline highly porous titanium(IV) dicarboxylate. J. Am. Chem. Soc. 131, 10857–10859.
Moon, G.-h, Kim, D.-h, Kim, H.-i, Bokare, A.D., Choi, W., 2014. Platinum-like behavior of reduced graphene oxide as a cocatalyst on TiO_2 for the efficient photocatalytic oxidation of arsenite. Environ. Sci. Technol. Lett. 1, 185–190.
Oseghe, E.O., Ofomaja, A.E., 2018. Facile microwave synthesis of pine cone derived C-doped TiO_2 for the photodegradation of tetracycline hydrochloride under visible-LED light. J. Environ. Manag. 223, 860–867.
Parayil, S.K., Kibombo, H.S., Koodali, R.T., 2013. Naphthalene derivatized TiO_2–carbon hybrid materials for efficient photocatalytic splitting of water. Catal. Today 199, 8–14.
Sankar Ganesh, M.N.R., Ponnusamy, S., Muthamizhchelvan, C., Kawasaki, S., Shimura, Y., Hayakawa, Y., 2018. Enhanced photon collection of high surface area carbonate-doped mesoporous TiO_2 nanospheres for dye sensitized solar cells applications. Mater. Res. Bull. 101, 353–362.
Shao, P., Tian, J., Zhao, Z., Shi, W., Gao, S., Cui, F., 2015. Amorphous TiO_2 doped with carbon for visible light photodegradation of rhodamine B and 4-chlorophenol. Appl. Surf. Sci. 324, 35–43.
Shi, X., Zhang, Z., Du, K., Lai, Y., Fang, J., Li, J., 2016. Anatase TiO_2@C composites with porous structure as an advanced anode material for Na ion batteries. J. Power Sources 330, 1–6.
Shu Wang, L.Z., Bai, Lina, Yan, Junmin, Jiang, Qing, Lian, Jianshe, 2014. Enhancing photocatalytic activity of disorderengineered C-TiO_2 and TiO_2 nanoparticles. J. Mater. Chem. A 2, 7439–7445.
Song, L., Jing, W., Chen, J., Zhang, S., Zhu, Y., Xiong, J., 2018. High reusability and durability of carbon-doped TiO_2/carbon nanofibrous film as visible-light-driven photocatalyst. J. Mater. Sci. 54, 3795–3804.
Sun, Y.Y., Zhang, S., 2016. Kinetics stabilized doping: computational optimization of carbon-doped anatase TiO_2 for visible-light driven water splitting. Phys. Chem. Chem. Phys. 18, 2776–2783.
Valero-Romero, M.J., Santaclara, J.G., Oar-Arteta, L., van Koppen, L., Osadchii, D.Y., Gascon, J., Kapteijn, F., 2019. Photocatalytic properties of TiO_2 and Fe-doped TiO_2 prepared by metal organic framework-mediated synthesis. Chem. Eng. J. 360, 75–88.
Wang, X., Lim, T.T., 2010. Solvothermal synthesis of C-N codoped TiO_2 and photocatalytic evaluation for bisphenol A degradation using a visible-light irradiated LED photoreactor. Appl. Catal. B Environ. 100, 355–364.
Wang, P., Li, Y., Liu, Z., Chen, J., Wu, Y., Guo, M., Na, P., 2017. In-situ deposition of Ag_3PO_4 on TiO_2 nanosheets dominated by (001) facets for enhanced photocatalytic activities and recyclability. Ceram. Int. 43, 11588–11595.
Wang, T., Nie, C., Ao, Z., Wang, S., An, T., 2020. Recent progress in g-C_3N_4 quantum dots: synthesis, properties and applications in photocatalytic degradation of organic pollutants. J. Mater. Chem. A 8, 485–502.
Wang, S., Pan, L., Song, J.-J., Mi, W., Zou, J.-J., Wang, L., Zhang, X., 2015. Titanium-defected undoped anatase TiO_2 with p-type conductivity, room-temperature ferromagnetism, and remarkable photocatalytic performance. J. Am. Chem. Soc. 137, 2975–2983.
Wang, P.F., Zhou, Q., Xia, Y., Zhan, S., Li, Y., 2018. Understanding the charge separation and transfer in mesoporous carbonate-doped phase-junction TiO_2 nanotubes for photocatalytic hydrogen production. Appl. Catal. B Environ. 225, 433–444.
Wu, M., He, X., Jing, B., Wang, T., Wang, C., Qin, Y., Ao, Z., Wang, S., An, T., 2020. Novel carbon and defects co-modified g-C_3N_4 for highly efficient photocatalytic degradation of bisphenol A under visible light. J. Hazard. Mater. 384, 121323.
Wu, M., Lv, H., Wang, T., Ao, Z., Sun, H., Wang, C., An, T., Wang, S., 2018. Ag_2MoO_4 nanoparticles encapsulated in g-C_3N_4 for sunlight photodegradation of pollutants. Catal. Today 315, 205–212.
Xiang, Q., Lv, K., Yu, J., 2010. Pivotal role of fluorine in enhanced photocatalytic activity of anatase TiO_2 nanosheets with dominant (001) facets for the photocatalytic degradation of acetone in air. Appl. Catal. B Environ. 96, 557–564.
Xia, D., Shen, Z., Huang, G., Wang, W., Yu, J.C., Wong, P.K., 2015. Red phosphorus: an earth-abundant elemental photocatalyst for "green" bacterial inactivation under visible light. Environ. Sci. Technol. 49, 6264–6273.
Yu, J., Dai, G., Xiang, Q., Jaroniec, M., 2011. Fabrication and enhanced visible-light photocatalytic activity of carbon self-doped TiO_2 sheets with exposed {001} facets. J. Mater. Chem. 21, 1049–1057.
Yu, F., Wang, L., Xing, Q., Wang, D., Jiang, X., Li, G., Zheng, A., Ai, F., Zou, J.-P., 2019. Functional groups to modify g-C_3N_4 for improved photocatalytic activity of hydrogen evolution from water splitting. Chin. Chem. Lett. 31, 1648–1653. https://doi.org/10.1016/j.cclet.2019.08.020.
Yu, S., Yun, H.J., Kim, Y.H., Yi, J., 2014. Carbon-doped TiO_2 nanoparticles wrapped with nanographene as a high performance photocatalyst for phenol degradation under visible light irradiation. Appl. Catal. B Environ. 144, 893–899.
Yu, L., Zhang, X., Li, G., Cao, Y., Shao, Y., Li, D., 2016. Highly efficient $Bi_2O_2CO_3$/BiOCl photocatalyst based on heterojunction with enhanced dye-sensitization under visible light. Appl. Catal. B Environ. 187, 301–309.
Yu, H., Zhao, Y., Zhou, C., Shang, L., Peng, Y., Cao, Y., Wu, L.-Z., Tung, C.-H., Zhang, T., 2014. Carbon quantum dots/TiO_2 composites for efficient photocatalytic hydrogen evolution. J. Mater. Chem. A 2, 3344.
Zhang, T., Lin, W., 2014. Metal–organic frameworks for artificial photosynthesis and photocatalysis. Chem. Soc. Rev. 43, 5982–5993.
Zhang, J., Li, M., Feng, Z., Chen, J., Li, C., 2006. U.V. Raman spectroscopic study on TiO_2. I. Phase transformation at the surface and in the bulk. J. Phys. Chem. B 110, 927–935.
Zhang, W., Xiao, X., Zheng, L., Wan, C., 2015. Fabrication of TiO_2/MoS_2@zeolite photocatalyst and its photocatalytic activity for degradation of methyl orange under visible light. Appl. Surf. Sci. 358, 468–478.
Zhang, G., Zhang, Y.C., Nadagouda, M., Han, C., O'Shea, K., El-Sheikh, S.M., Ismail, A.A., Dionysiou, D.D., 2014. Visible light-sensitized S, N and C co-doped polymorphic TiO_2 for photocatalytic destruction of microcystin-LR. Appl. Catal. B Environ. 144, 614–621.
Zhang, Y., Zhao, Z., Chen, J., Cheng, L., Chang, J., Sheng, W., Hu, C., Cao, S., 2015. C-doped hollow TiO_2 spheres: in situ synthesis, controlled shell thickness, and superior visible-light photocatalytic activity. Appl. Catal. B Environ. 165, 715–722.
Zhou, Y., Zhang, L., Tao, S., 2018. Porous TiO_2 with large surface area is an efficient catalyst carrier for the recovery of wastewater containing an ultrahigh concentration of dye. RSC Adv. 8, 3433–3442.